

IRAC photometric analysis and the mid-IR photometric properties of Lyman-break galaxies

G. E. Magdis,¹★ D. Rigopoulou,¹ J.-S. Huang,² G. G. Fazio,² S. P. Willner² and M. L. N. Ashby²

¹Department of Physics, University of Oxford, Keble Road, Oxford OX1 3RH

²Harvard-Smithsonian Center for Astrophysics, 60 Garden Street, Cambridge, MA 02138, USA

Accepted 2008 January 24. Received 2008 January 23; in original form 2007 October 12

ABSTRACT

We present photometric analysis of deep mid-infrared (mid-IR) observations obtained by *Spitzer*/IRAC covering the fields Q1422+2309, Q2233+1341, DSF2237a,b, HDFN, SSA22a,b and B20902+34, giving the number counts and the depths for each field. In a sample of 751 Lyman-break galaxies (LBGs) lying in those fields, 443, 448, 137 and 152 are identified at 3.6-, 4.5-, 5.8-, 8.0- μ m IRAC bands, respectively, expanding their spectral energy distribution to rest-near-IR and revealing that LBGs display a variety of colours. Their rest-near-IR properties are rather inhomogeneous, ranging from those that are bright in IRAC bands and exhibit $[R] - [3.6] > 1.5$ colours to those that are faint or not detected at all in IRAC bands with $[R] - [3.6] < 1.5$ colours and these two groups of LBGs are investigated. We compare the mid-IR colours of the LBGs with the colours of star-forming galaxies and we find that LBGs have colours consistent with star-forming galaxies at $z \sim 3$. The properties of the LBGs detected in the 8- μ m IRAC band (rest-frame K band) are examined separately, showing that they exhibit redder $[R] - [3.6]$ colours than the rest of the population and that although in general, a multiwavelength study is needed to reach more secure results, IRAC 8- μ m band can be used as a diagnostic tool, to separate high z , luminous AGN-dominated objects from normal star-forming galaxies at $z \sim 3$.

Key words: galaxies: evolution – galaxies: high redshift – galaxies: statistics – cosmology: observations – infrared: galaxies.

1 INTRODUCTION

Observation and study of high-redshift galaxies is essential to constrain the history of galaxy evolution and give us a systematic and quantitative picture of galaxies in the early Universe, an epoch of rigorous star and galaxy formation. Large samples of high- z galaxies that have recently become available, play a key role to that direction and have revealed a zoo of different galaxy populations at $z \sim 3$. There are various techniques for detecting high- z galaxies involving observations in wavelengths that span from optical to far-infrared (far-IR). Among these, the three most efficient are (1) submillimetre blank field observations, using the Submillimetre Common-User Bolometer Array (SCUBA) on the James Clerk Maxwell Telescope (e.g. Hughes et al. 1998) or the Max Plank Millimetre Bolometer array (MAMBO, e.g. Bertoldi et al. 2000), taking advantage of the strong negative K -correction effect and revealing the population of the submillimetre galaxies at $z > 2$ (Chapman et al. 2000; Ivison et al. 2002; Smail et al. 2002) and (2) the U -band-dropout technique

(Steidel & Hamilton 1993; Steidel et al. 1999; Franx et al. 2003; Steidel et al. 2003; Daddi et al. 2004), sensitive to the presence of the 921-Å break, designed to select $z \approx 3$ galaxies and revealing the population of the Lyman-break galaxies (LBGs), (3) the near-IR (NIR) colour ($J - K > 2.3$ (Franx et al. 2003) and BzK [$(z - K)_{\text{AB}} - (B - z)_{\text{AB}} > -0.2$] (Daddi et al. 2004) selection for old and dusty galaxies at $2 < z < 3$ (distant red galaxies (DRGs) and BzK galaxies).

With recent deep optical and IR observations of these three types of galaxies, there has been considerable progress in understanding the relation between LBGs, SMGs, DRGs and BzK galaxies. Chapman et al. (2005) confirmed that some of the SCUBA galaxies have rest-frame ultraviolet (UV) colours typical of the LBGs. Using IRAC and MIPS observations, Huang et al. (2005) has shown that LBGs detected in MIPS 24- μ m band, [infrared luminous LBGs (ILLBG)] and cold SCUBA sources share similar [8.0] – [24] colours, while Rigopoulou et al. (2006) suggest that ILLBGs and SCUBA galaxies tend to have similar stellar masses and dust amount. A possible scenario is one in which submillimetre galaxies and LBGs form a continuum of objects with SMGs representing the reddest dustier and more intensively star-forming LBGs, but further

★E-mail: gem@astro.ox.ac.uk

investigation is required to establish a more secure link between these two populations.

LBGs constitute at the moment the largest and most well studied galaxy population at $z \sim 3$ (Steidel et al. 2003). Based on observations of the UV continuum emission, the predicted mean star formation rate of the LBGs is $20\text{--}50 M_{\odot} \text{ yr}^{-1}$ (assuming $H_0 = 70 \text{ km s}^{-1} \text{ Mpc}^{-1}$ and $q_0 = 0.5$, Pettini et al. 2001). This star formation rate increases significantly if corrected for dust attenuation, to a mean value of $\sim 100 M_{\odot} \text{ yr}^{-1}$. Correction for dust attenuation must be taken into account as there is clear evidence for the presence of significant amounts of dust in the galactic medium of LBGs (e.g. Sawicki & Yee (1998); Vija, Witt & Gordon 2003).

To investigate the amounts of dust in the LBGs, various techniques and observations spanning from optical to X-rays have been used. The techniques range from studies of optical line ratios (Pettini et al. 2001) to formal fits of the overall SED of LBGs based on various star formation history scenarios (e.g. Papovich, Dickinson & Ferguson 2001; Shapley et al. 2001, 2003) and X-ray stacking studies (e.g. Nandra et al. 2002; Reddy & Steidel 2004). All approaches agree that LBGs with higher star formation rates contain more dust (e.g. Adelberger & Steidel 2000; Reddy et al. 2006).

One of the most important properties of the population is the stellar mass of the galaxies. Stellar masses play a central role to the understanding of the evolution of the LBGs, as the co-moving stellar mass density at any redshift is the integral of the past star-forming activity and suffers fewer uncertainties than the star formation rate. Most of the attempts to estimate the stellar content of the LBGs were based on ground-based observations. As the observed optical band corresponds to rest-UV for galaxies at $z \sim 3$, most of the light emitted from the galaxy at these wavelengths is radiated from young and massive OB stars. Therefore, optical observations cannot be regarded as a robust tool to probe the stellar mass of the galaxy as they are sensitive only to recent star formation episodes rather than the stellar population that has accumulated over the galaxy's lifetime. Observations at longer wavelengths, i.e. rest-NIR (e.g. Bell & de Jong 2001), where the bulk of the stellar population radiates are essential to constrain the stellar content of the $z \sim 3$ galaxy population.

With the advent of the *Spitzer Space Telescope* (Werner et al. 2004) we now have access to longer wavelengths. The four IRAC bands onboard *Spitzer* (Fazio et al. 2004) and more particularly the fourth band at $8.0 \mu\text{m}$ allows us to observe the rest-frame K band where the bulk of the stellar population of a galaxy radiates and expand the SED of the galaxies from rest-UV to NIR. Thus, with IRAC data in hand we have a powerful tool to probe in a more secure way the stellar content of the LBGs. Recent results of adding IRAC photometry to stellar mass estimates have been presented in e.g. Barmby et al. (2004) for $z \sim 3$, Shapley et al. (2005) for BX/BM objects and Reddy et al. (2006) for $z \sim 2\text{--}3$. Also, IRAC colours combined with ground-based data, can enlighten the diversity of the

population revealing the existence of different subclasses of LBGs, and provide an insight to their physical properties such as the energy source that powers the LBGs.

This paper is organized as follows. Section 2 reviews the data of this study and presents the source extraction and the photometric analysis, as well as, the differential number counts for each field. Section 3 focuses on the mid-IR identifications of LBGs, while in Section 4 the rest-frame NIR photometric properties of the LBGs are discussed. Finally, Section 5 summarizes the main results of this study. All magnitudes appearing in this study are in AB magnitude system.

2 Spitzer OBSERVATIONS

The data for this study have been obtained with the Infrared Array Camera (IRAC) (Fazio et al. 2004) on the board *Spitzer Space Telescope*. The majority of our data are part of the IRAC Guaranteed Time Observation programme (GTO, PI G. Fazio) and include the fields: Q1422+2309 (Q1422), DSF2237a,b (DSF), Q2233+1341 (Q2233), SSA22a,b (SSA22) and B20902+34 (B0902) while data for the HDFN come from the Great Observatories Origin Deep Survey programme (GOODS, PIM. Dickinson). IRAC has the capability of observing simultaneously in four, $3.6\text{-, }4.5\text{-, }5.8\text{- and }8.0\text{-}\mu\text{m}$ bands, covering one $5 \times 5\text{-arcmin}^2$ field at 3.6 and $5.8 \mu\text{m}$ and an adjacent $5 \times 5\text{-arcmin}^2$ field at 4.5 and $8.0 \mu\text{m}$. All fields discussed here were covered by IRAC at 3.6 , 4.5 , 5.8 and $8.0 \mu\text{m}$. In general there is a big overlap of the observing part of the sky between the four bands for each field. This overlap is maximum between the bands 1 and 3 (set 1), and bands 2 and 4 (set 2). While it can be small between set 1 and set 2 for some fields, to the point of 50 per cent. Field positions, dates, covered area and exposure time for each observation are summarized in Table 1, while the expected AB magnitudes at which the observations for those fields reach a 5σ point-source sensitivity limit are given in Table 2.

The IRAC Basic Calibrated Data (BCD) delivered by the Spitzer Science Centre include flat-field corrections, dark subtraction, linearity correction and flux calibration. The BCD data were further processed by our team's own refinement routines. This additional reduction steps include distortion corrections, pointing refinement, mosaicking and cosmic ray removal by sigma clipping. Finally, the fields that were observed more than one time and at different position angles, removal of instrumental artefacts during mosaicking was significantly facilitated.

2.1 Source extraction

Source extraction was based on fitting point spread functions (PSFs) in each field. Because the depth of the observations varies from field to field and the sensitivity of IRAC drops significantly for the $5.8\text{- and }8.0\text{-}\mu\text{m}$ bands, different PSFs were chosen for each field and each band. The fact that those fields are very crowded combined

Table 1. Details of the fields covered by this study.

| Fields | RA/Dec. | Date | Area (deg^2) | Exposure time (h) |
|------------|--|------------|-------------------------|-------------------|
| HDFN | $12^{\text{h}}36^{\text{m}}49\overset{\text{s}}{.}6 +62^{\circ}1327$ | 2004-05-16 | 0.096 | ~ 95.27 |
| DSF2237a,b | $22^{\text{h}}39^{\text{m}}06\overset{\text{s}}{.}7 +12^{\circ}0056$ | 2004-07-04 | 0.0173 | ~ 1.5 |
| SSA22a,b | $22^{\text{h}}17^{\text{m}}24\overset{\text{s}}{.}1 +00^{\circ}1132$ | 2006-07-12 | 0.125 | ~ 1.5 |
| Q1422+2309 | $14^{\text{h}}24^{\text{m}}40\overset{\text{s}}{.}7 +23^{\circ}0019$ | 2004-01-10 | 0.024 | ~ 1.0 |
| Q2233+1341 | $22^{\text{h}}36^{\text{m}}23\overset{\text{s}}{.}3 +13^{\circ}5907$ | 2003-12-20 | 0.017 | ~ 1.0 |
| B20902+34 | $09^{\text{h}}05^{\text{m}}22\overset{\text{s}}{.}5 +34^{\circ}0822$ | 2005-05-07 | 0.017 | ~ 1.0 |

Table 2. Details on the source extraction and photometry in each field and each IRAC band.

| Properties/field | HDFN | Q1422 | Q2233 | SSA22 | DSF2237 | B0902 |
|--------------------------------|--------|-------|-------|--------|---------|-------|
| 3.6 μm | | | | | | |
| 5 σ limit ^a | 25.5 | 22.9 | 22.9 | 23.2 | 23.2 | 22.9 |
| Magnitude limit ^b | 27.8 | 24.8 | 24.7 | 25.1 | 25.2 | 24.7 |
| Sources extracted ^c | 25 615 | 4105 | 2615 | 28 219 | 3403 | 3112 |
| Completeness 50% per cent | 24.9 | 23.1 | 23.1 | 23.7 | 24.0 | 23.4 |
| 4.5 μm | | | | | | |
| 5 σ limit | 25.2 | 22.9 | 22.9 | 23.1 | 23.1 | 22.9 |
| Magnitude limits | 27.5 | 24.5 | 24.5 | 24.9 | 25.1 | 24.5 |
| Sources extracted | 24 531 | 3994 | 2808 | 28 253 | 3846 | 3005 |
| Completeness 50 per cent | 24.9 | 23.1 | 23.1 | 23.7 | 23.7 | 23.4 |
| 5.8 μm | | | | | | |
| 5 σ limit | 23.9 | 21.5 | 21.5 | 22.2 | 22.2 | 21.5 |
| Magnitude limits | 26.1 | 22.6 | 22.5 | 23.1 | 23.1 | 22.6 |
| Sources extracted | 15 527 | 2063 | 1719 | 16 356 | 1818 | 1219 |
| Completeness 50 per cent | 23.4 | 21.6 | 21.9 | 22.2 | 22.6 | 21.6 |
| 8.0 μm | | | | | | |
| 5 σ limit | 23.8 | 21.4 | 21.4 | 22.2 | 22.2 | 21.4 |
| Magnitude limits | 26.1 | 22.6 | 22.4 | 23.1 | 23.1 | 22.5 |
| Sources extracted | 14 315 | 1658 | 1172 | 14 192 | 1392 | 1119 |
| Completeness 50 per cent | 23.4 | 21.6 | 21.9 | 22.2 | 22.2 | 21.6 |

^aExpected AB magnitudes at which the observations reach a 5 σ point-source sensitivity. ^bMagnitude limits for source extraction.

^cNumber of extracted sources. ^dMagnitude at which the completeness of the source extraction reaches 50 per cent.

with the small number of stars in those fields, made the selection of the PSFs very challenging. The situation was more complicated for bands 3 and 4 where the noise increases significantly. To accurately compute the best PSF, we used as many point sources located throughout the IRAC images as possible. The construction of PSFs was iterative taking into account not only isolated stars, but also stars with faint objects close to them. To produce the optimum PSF we developed an IDL code that uses the stars we select as appropriate for PSFs, subtracts objects that are blended or near to them, and creates a ‘clean’ average PSF.

With PSFs derived as above, we performed source extraction using STARFIND. The final PSF was fitted in the image, searching the input images for local density maxima with half-widths at half-maxima of the PSFs, and peak amplitudes greater than a given threshold above the local background. With a full width at half-maximum of the PSF of 1.8–2.2 arcsec, virtually all objects are unresolved. The detection limits varied from field to field and from band to band according to the depth of the observation and the sensitivity of the observed band. The source extraction for each field and each IRAC band was repeated with slightly varied parameters till the optimum source extraction was achieved (the results of each run were inspected by eye to check if the extraction was shallow resulting in missing real sources, or if we had gone to deep and noise was picked as sources). The threshold was highly dependent on the exposure time of the observations. For fields of equal exposure time (i.e. depth) the same detection thresholds were used, while for deeper observations the threshold was lower. The limiting magnitudes of the performed source extraction and the number of objects detected in each field and each IRAC band are summarized in Table 2.

2.2 Completeness and photometry

The uncertainties and the completeness of the source extraction in the IRAC bands magnitudes were estimated from an analysis employing Monte Carlo simulations. In average 6000 artificial sources

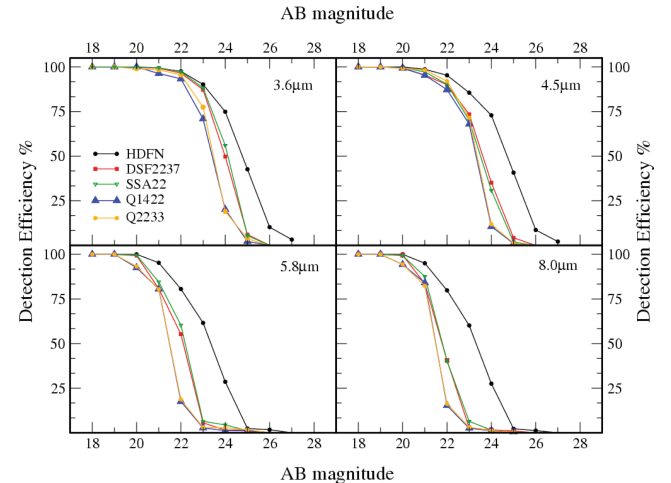


Figure 1. The incompleteness curve for all fields and IRAC bands (B0902 is excluded for presentation purposes, but it follows the incompleteness curve of the fields with equal depth, i.e. Q1422 and Q2233). Each field is indicated by different symbol and colour. The incompleteness in the four IRAC bands shows the usual rapid increase near the magnitude limit of the images and declines sharply near the faint limits. Furthermore, there is significant improvement in fields with larger exposure time, with the completeness of HDFN falling to 50% at a magnitude of ~ 25 at 3.6 μm , while for SSA22 at a magnitude of ~ 23.9 .

were added to each image, and were extracted in the same manner as the real sources. The dispersion between input and recovered magnitudes and number of objects provides a secure estimation of the detection rate and the photometric error in each magnitude bin. The incompleteness curve for each individual field and each IRAC band are illustrated in Fig. 1 while the depth at which the completeness of our source extracting method reaches 50 per cent are summarized in Table 2. The incompleteness in all four IRAC bands shows the usual rapid increase near the magnitude limit of

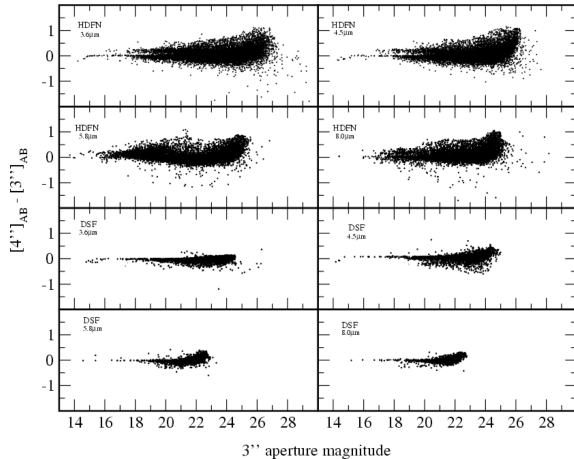


Figure 2. $[4 \text{ arcsec}] - [3 \text{ arcsec}]$ versus $[3 \text{ arcsec}]$ magnitude for the objects of the fields HDFN and DSF. The strong concentration of the residual around zero indicates that the applied aperture corrections are correct.

the images and declines sharply near the faint limits. Furthermore, there is significant improvement in fields with larger exposure times, with the completeness of HDFN falling to 50 per cent at a magnitude of ~ 25 at $3.6 \mu\text{m}$, while for SSA22 at a magnitude of ~ 23.9 .

For the photometric analysis, PSF fitting and aperture photometry using a 3, 4.5 and 6 arcsec diameter aperture was performed. The aperture fluxes in each band were subsequently corrected to total fluxes using known PSF growth curves from Fazio et al. (2004) and Huang et al. (2005). Fig. 2 shows the residual of the 4 arcsec minus the 3 arcsec diameter aperture photometry over the 3 arcsec diameter aperture photometry for IRAC bands of fields HDFN and DSF. The strong concentration of the residual around zero indicates that the applied aperture corrections are correct and within the uncertainty of our photometry. This good agreement also holds between PSF and aperture photometry. The magnitude–error relation is shown in Fig. 3 for three fields, HDFN, Q1422 and SSA22. We choose to plot these three fields as they cover the whole range of depths

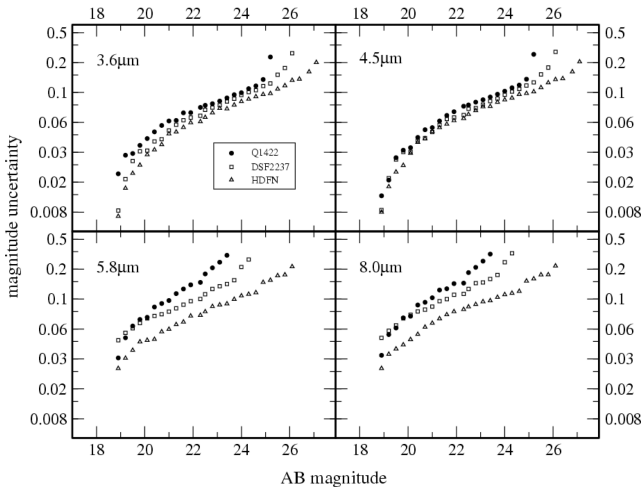


Figure 3. The magnitude–error relation for three fields, HDFN (triangles), Q1422 (filled circles) and SSA22 (squares). It should be noted that the y-axis is in log scale for comparison purposes. DSF has comparable photometric error bars with SSA22, while the magnitude–error relation for both Q2233 and B0902 follows that of Q1422.

of our observations. DSF has comparable photometric error bars with SSA22, while the magnitude–error relation for both Q2233 and B0902 follows that of Q1422.

The four catalogues for the IRAC wavelengths were matched by position to create a single master catalogue of IRAC sources for each field. While the entire catalogues will be presented in a forthcoming paper anyone interested in those should contact the author.

2.3 Number counts

The observations span 2.5 yr and a factor of 95 in exposure time (i.e. depth). A reliable indicator that all fields were treated in the same manner are the number counts. Fig. 4 shows the differential number counts in the four IRAC bandpasses including all sources, stars and galaxies in each field versus the magnitude bins. We plot the number counts for magnitudes at which the completeness is >50 per cent, while the uncertainty in the number counts is based on Poisson noise. There is an excellent agreement between the number counts of the fields in the bright end and this agreement stands in the faint end between fields of equal exposure time. As expected the number counts peak in fainter magnitudes for fields with larger exposure times, while for fields of similar depth (Q2233, B2090, Q1422 and DSF2233, SSA22) the turning point is equal. It should be noted that the number counts of HDFN, despite the 95 h of integration, appear to peak (completeness ~ 50 per cent) only 1.5–2 AB magnitude deeper than the fields with 1.5 h of exposure time. On the other hand, the large difference in the exposure time between HDFN and the rest fields becomes very significant for the number counts in magnitudes where the completeness is 50 per cent, as for shallower fields the number counts decline very steeply, compared to HDFN.

In Fig. 5 we compare the differential number counts of the Extended Groth Strip (EGS) by Fazio et al. (2004), *Chandra Deep Field-South* (CDFS) area by Franceschini et al. (2006) (only for the $3.6\text{-}\mu\text{m}$ band) and of HDFN derived by this study. The exposure time for the EGS and CDFS is ~ 1.5 and ~ 46 h, respectively. There is a very good agreement between the results with an excess in the faint end for our data, which is due to the very deep observations of HDFN.

3 MID-INFRARED IDENTIFICATION OF LBGs

Steidel et al. (2003) published a catalogue of 1261 LBGs in the six fields while our observations covered 751 LBGs in at least one IRAC waveband. The sample of 751 LBGs, consists of three categories of objects. Those that have confirmed spectroscopic redshift (through follow up ground-based optical/NIR spectroscopy, Steidel et al. 2003) and are identified as galaxies at $z \sim 3$ (LBGs-z) or classified as active galactic nuclei (AGN)/QSO and, those that do not have spectroscopic redshifts. In total, 321 LBGs-z, 12 AGN/QSO and 435 LBGs without spectroscopic redshift are covered. Out of these, 625 were covered by IRAC at all four wavelengths constituting our main LBG sample, while an additional 50 LBGs were covered at $[3.6]$ and $[5.8]\text{ }\mu\text{m}$ and 93 at $[4.5]$ and $[8.0]\text{ }\mu\text{m}$. Those additional LBGs were added to our statistical analysis when appropriate. To identify LBGs in the IRAC images Steidel’s catalogue was matched to the IRAC source lists. The *Spitzer* astrometry is aligned to the ESO Imaging Survey with a typical accuracy of 0.5 arcsec (Arnouts et al. 2001).

We searched for counterparts within a 1 arcsec diameter separation centred on the optical position. As the typical size for an LBG is 1 arcsec in most cases the LBGs were clearly identified. Given

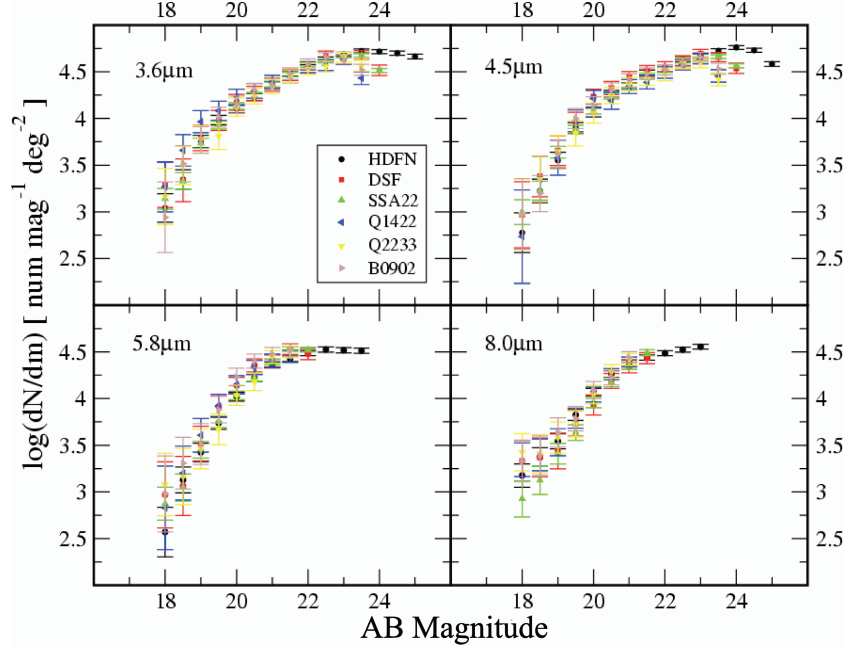


Figure 4. Differential number counts in the four IRAC bandpasses including all sources, stars and galaxies. Counts in the six fields are indicated by different colours and symbols. We plot the number counts only for magnitudes where the completeness is >50 per cent. There is an excellent agreement in the bright end for all the fields and in the faint end for observations of equal exposure time (i.e. depth). The error bars represent the Poisson noise.

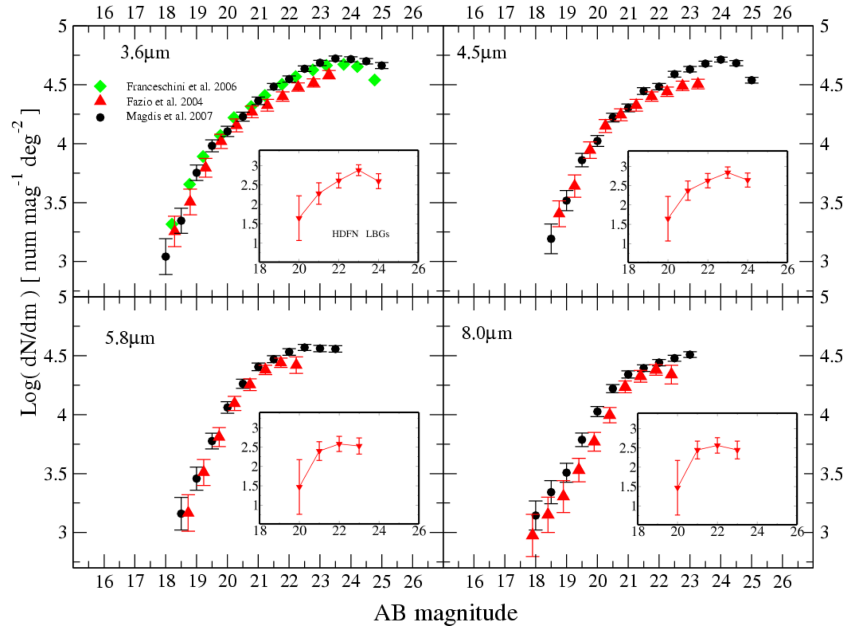


Figure 5. Comparison between differential number counts in the four IRAC bandpasses for HDFN (black circles) from this study, EGS (red triangles) from Fazio et al. (2004) and CDFS (green diamonds) from Franceschini et al. (2006) (only for 3.6 μm). The enclosed plots show the number counts of the detected LBGs in HDFN.

the depth of the IRAC images, some associations with LBGs are likely to be spurious. The number of objects with surface density n located within a distance d from a random position on the sky is given by $S = \pi n d^2$ (e.g. Lilly et al. 1999). The surface density $n(m)$ for each field at each magnitude is given by the differential number counts as discussed in the previous section, and the value d was set to 1 since for the identification of LBGs in IRAC images, a radius of 1 arcsec was used for searching for NIR counterpart. The number

of detected LBGs in each magnitude bin was then calculated. We applied the mathematic formula described above and derived the expected spurious objects for each of the three categories of fields and each IRAC bandpass. The results are shown in Fig. 6, where the magnitude distribution of the detected LBGs is overplotted with that of the expected spurious objects. The high ratio of detected LBGs over the expected spurious objects makes the majority of our identifications secure.

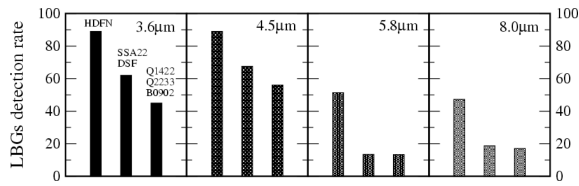


Figure 6. Detection rate of LBGs in the several fields and at each IRAC band. The fields are grouped according to the depth, with HDFN being the deepest field, SSA22 and DSF having intermediate depth and Q1422, Q2233 and B0902 being the fields with the least exposure time. The detection rate is strongly dependent on the depth of the observations.

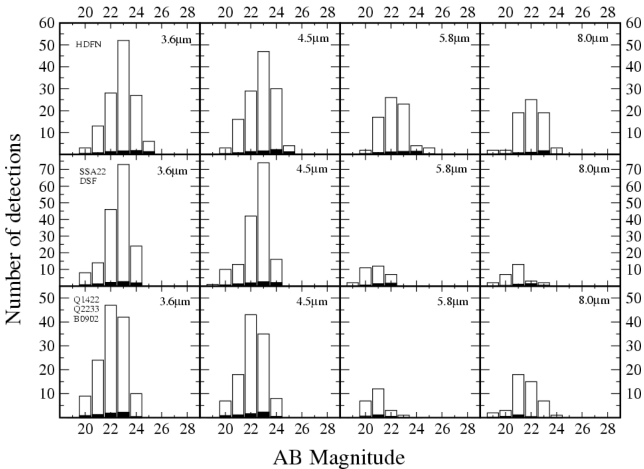


Figure 7. Magnitude distribution of detected (empty bars) and expected spurious detections for each IRAC bandpass. The fields are grouped into three sets according to the depth of their observation. The top panel shows the distribution for the HDFN, the middle for the fields SSA22 and DSF while the bottom for Q1422, Q2233 and B0902.

The detection rate of the LBGs is highly dependent on the depth of the observation, with fields of equal depth having equal detection rates. Therefore, the six fields are divided in three groups according to their depth. The first category includes only the HDFN as it is the field with the largest exposure time. In the second category the fields of intermediate depth, i.e. SSA22 and DSF are included, while the shallowest fields, Q1422, Q2233 and B0902 constitute the third category. Fig. 7 shows the detection rate of LBGs at each of these categories and for all IRAC bandpasses. Apart from the large difference in the detection rate among several fields, we note the large decline in the detection rate at 5.8- and 8.0- μm bands compared to 3.6 and 4.5 μm for images of the same field. For example, in HDFN the detection rate reaches 90 per cent for the first two IRAC bands while it drops to 50 per cent for 5.8 and 8.0 μm . Table 3 summarizes the LBGs covered/detected in each IRAC band while the total number of detections in each group of fields and each IRAC band are given in Table 4.

Table 3. LBGs detected/covered in all fields and each IRAC band.

| Band/type | LBG | | LBG-z | | LBG-non | | AGN | |
|-------------------|-----|-----|-------|-----|---------|-----|-----|----|
| | D | C | D | C | D | C | D | C |
| 3.6 μm | 443 | 658 | 192 | 263 | 241 | 385 | 10 | 10 |
| 4.5 μm | 448 | 708 | 195 | 289 | 243 | 409 | 10 | 10 |
| 5.8 μm | 137 | 658 | 54 | 263 | 75 | 385 | 8 | 10 |
| 8.0 μm | 152 | 708 | 66 | 289 | 77 | 409 | 9 | 10 |

Table 4. Detected LBGs in fields categorized by depth, for all IRAC band-passes.

| Band/type | HDFN | SSA22 and DSF2237 | Q1422, Q2233 and B0902 |
|-------------------|------|-------------------|------------------------|
| 3.6 μm | 131 | 170 | 142 |
| 4.5 μm | 130 | 199 | 120 |
| 5.8 μm | 75 | 32 | 30 |
| 8.0 μm | 69 | 37 | 47 |

Table 5. Detected/covered LBGs that are covered by all four IRAC bands.

| Band/type | LBG | | LBG-z | | LBG-non | | AGN | |
|-------------------|-----|-----|-------|-----|---------|-----|-----|---|
| | D | C | D | C | D | C | D | C |
| 3.6 μm | 417 | 615 | 183 | 248 | 226 | 359 | 8 | 8 |
| 4.5 μm | 394 | 615 | 173 | 248 | 213 | 359 | 8 | 8 |
| 5.8 μm | 129 | 615 | 51 | 248 | 71 | 359 | 7 | 8 |
| 8.0 μm | 143 | 615 | 65 | 248 | 70 | 359 | 8 | 8 |

To examine the rest-NIR photometric properties of the LBGs in a more complete way, in this paper we will focus on the 625 LBGs that have been covered from all four IRAC bands. Out of these 625 LBGs about 425 are detected with IRAC at 3.6 μm , 401 at 4.5 μm , 136 at 5.8 μm and 149 at 8.0 μm . Of these, 258 are LBGs-z, eight are classified as AGN/QSO and 359 do not have spectroscopic redshift. In Table 5 we summarize the covered/detected LBGs that overlap between the IRAC bands.

4 THE PHOTOMETRIC PROPERTIES OF LBGS

4.1 The spectral energy distribution of LBGs

With the *Spitzer* IRAC data we extend the spectral energy distribution (SED) of the LBGs to rest-frame NIR and improve dramatically our understanding of the nature of LBGs. Fig. 8 shows the rest-UV/optical/NIR SEDs of all LBGs of the current sample with confirmed spectroscopic redshift, while the enclosed plot shows the SEDs of the LBGs-z detected in HDFN. UV/optical data are obtained from Steidel et al. (2003), while IRAC data come from the present work. While the rest-UV/optical show little variation (2–3 mag), the rest-frame NIR colour spread over 6 mag. The addition of IRAC bands reveals for the first time that LBGs display a variety of colours and their rest-NIR properties are rather inhomogeneous, ranging from

(i) those that are bright in IRAC bands and exhibit $R - [3.6] > 1.5$ colours; their SEDs are rising steeply towards longer wavelengths and based on their $R - [3.6]$ we call them ‘red’ LBGs-z, to

(ii) those that are faint or not detected at all in IRAC bands with $R - [3.6] < 1.5$ colour. Their SEDs are rather flat from the far-UV to the NIR with marginal IRAC detections and as they exhibit bluer $R - [3.6]$ colours we call them ‘blue’ LBGs-z.

Out of the whole sample, 3 per cent of LBGs display $R - [3.6] > 4$, similar to the extremely red objects discussed by e.g. Wilson et al. 2004.

To avoid conclusions driven by selection effects and depth variance between the several fields, the sample coming from the HDFN was separately investigated from the other fields. The comparison of the two samples provides a simple way to understand the impact

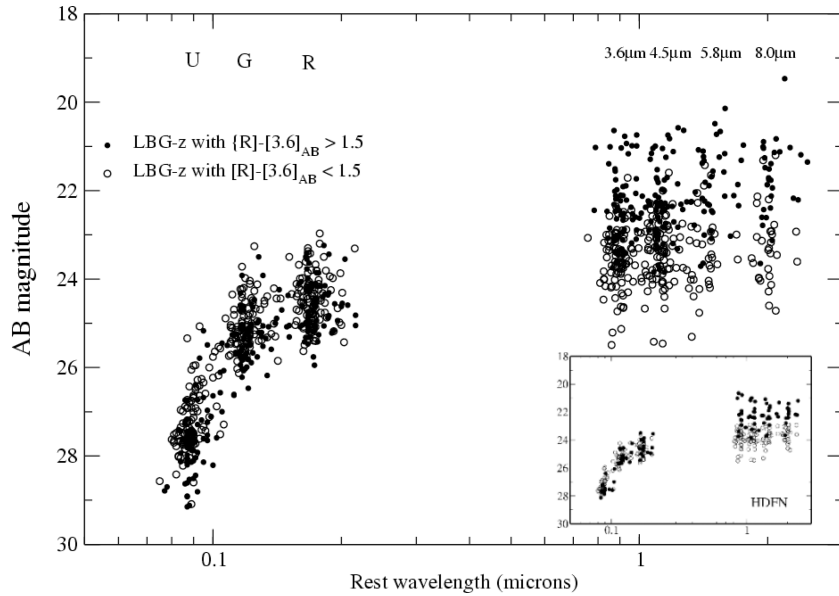


Figure 8. SED for LBGs with spectroscopic redshifts and classified as galaxies. Empty circle represent LBGs with $R - [3.6] < 1.5$, while filled circles represent LBGs with $R - [3.6] > 1.5$, revealing that the rest-NIR of the population displays a wide range of colours. The enclosed plot shows the same information but only for LBGs in HDFN.

that the depth of the observation has in our sample, and therefore derive more secure global interpretations.

For LBGs with $R - [3.6] > 1.5$ in HDFN, the median value (taking into account upper limits) of $[3.6]$ and $R - [3.6]$ is 22.15 ± 0.078 and 2.31 ± 0.125 , respectively. For those with $R - [3.6] < 1.5$ we get median values of 23.84 ± 0.141 and 0.898 ± 0.227 while for the whole sample the derived values are 23.39 ± 0.121 and 1.212 ± 0.201 . Kolmogorov–Smirnov test (KS test) showed that the maximum difference between the cumulative distributions, D , for the $[3.6]$ values of the two samples is 0.77 with a corresponding p -value of 0.000 14, suggesting a significant difference in their IRAC 3.6- μm colours with the ‘red’ LBGs being significantly brighter.

On the other hand the median value of $[3.6]$ and $R - [3.6]$ for the LBGs in the shallower fields is 22.51 ± 0.095 and 1.915 ± 0.117 for those with $R - [3.6] > 1.5$, 23.33 ± 0.120 and 0.975 ± 0.214 those with $R - [3.6] < 1.5$ while for the whole sample the derived median values are 23.02 ± 0.098 and 1.372 ± 0.195 . KS test showed again that there is a significant difference between the $[3.6]$ colours of the ‘blue’ and ‘red’ LBGs, in agreement with the results derived from LBGs in HDFN.

Fig. 9 shows the average SEDs of these two groups of LBGs-z and that of the AGN. The selected LBGs for this plot are detected in all four IRAC bands, have a similar redshift ($2.9 < z < 3.1$) and are all drawn from the LBG sample of HDFN. The addition of the IRAC data (i.e. rest-NIR for our sample) reveals the difference in the SEDs of these three categories of objects becomes, implying the two groups of LBGs-z do not share the same properties. Further investigation of the physical properties of these two groups employing stellar synthesis population models, will follow in a forthcoming paper.

Although the large difference in the depth of the several observations does not seem to affect the derived properties of the population, it can affect the proportion of ‘red’–‘blue’ LBGs in each sample. Fig. 10 shows the $R - [3.6]$ colours distribution of the detected LBGs for HDFN and for the rest of the fields. While the distribution for LBGs with $R - [3.6] > 1$ is similar for the two samples, there is an excess of LBGs with $R - [3.6] < 1$ in the HDFN. The

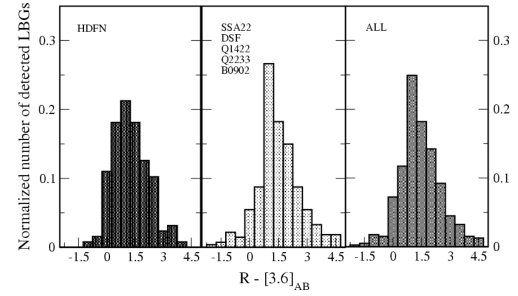


Figure 9. $R - [3.6]$ colour distribution of detected LBGs, normalized to the total number of detection for each set of fields. The left-hand panel describes the distribution for HDFN, the middle panel for the rest of the fields and the right-hand panel for the whole sample of LBGs.

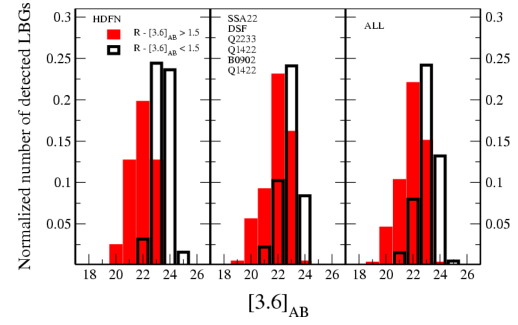


Figure 10. Normalized $[3.6]$ mag distribution of detected LBGs, for LBGs with $R - [3.6] > 1.5$ (red bars) and $R - [3.6] < 1.5$ (black bars). The left-hand panel describes the distribution for HDFN, the middle panel for the rest of the fields and the right-hand panel for the whole sample of LBGs.

median value of $[3.6]$ of the LBGs in HDFN with $R - [3.6] < 1$ is 24.31 ± 0.16 , but as shown in Fig. 7 the detection rate at the shallower fields is on average half of that in the HDFN affecting mainly the detection of faint LBGs. This can be easily understood

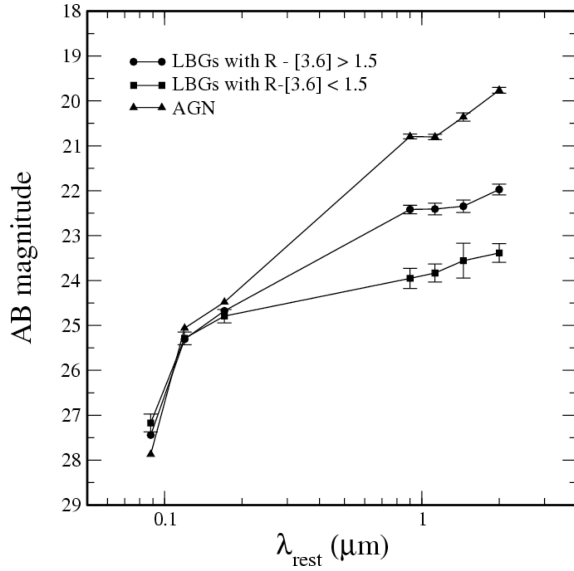


Figure 11. Average SEDs for AGN (triangles), LBGs-z (squares) with $R - [3.6] < 1.5$ and LBGs-z with $R - [3.6] > 1.5$ (circles). We restrict our sample to objects of redshift $2.9 < z < 3.1$.

from Fig. 6. In all but HDFN fields, there are very few or zero detections at magnitudes fainter than 24. It is therefore expected that LBGs with $R - [3.6] < 1.5$ are under-represented in the sample of the shallow fields. To quantify this underdetection of ‘blue’ LBGs in the shallow fields we compare the fraction of population with $R - [3.6] < 1$ (where the depth of the observation becomes significant) between the two samples. LBGs with $R - [3.6] < 1.0$ in HDFN accounts for the ~ 31.3 per cent of the total detected LBGs while in the shallower fields this fraction drops to ~ 17.7 per cent. Therefore, a simple assumption would be that ‘blue’ LBGs in the shallower fields are under-represented by ~ 14 per cent, which corresponds to ~ 45 missing ‘blue’ LBGs. On the other hand, LBGs with $R - [3.6] > 1.5$ have similar mean values of $[3.6]$ in all fields (22.15 for HDF and 22.51 for the rest), bright enough even for the shallow fields to have at least comparable detection efficiency with that of HDFN. The above discussion is clearly demonstrated in Fig. 11 where we present the $[3.6]$ mag distribution of LBGs with $R - [3.6] > 1.5$ and $R - [3.6] < 1.5$, for the two individual samples as well as for whole sample.

4.2 The IRAC 8- μm sample

From the whole LBG sample detected in 3.6- and 4.5- μm LBGs, about ~ 34 per cent are detected in longer wavelengths. This is what we call the sample of the 8- μm LBGs. In total 8- μm counterparts were detected in 152 LBGs and the detection rate is significantly lower when compared to that at 3.6 and 4.5 μm . The question that should be answered is how the 8- μm LBGs are distributed between the $R - [3.6] < 1.5$ and $R - [3.6] > 1.5$ LBGs and how this distribution is affected by the different depths of observations. Again, useful conclusion can be derived from the comparison of the two sets of fields (HDFN – the rest). The detection rate of 8- μm LBGs in HDFN is ~ 50 per cent while for the rest fields falls dramatically to ~ 17 per cent. A simple assumption would be that in the shallower fields the 8- μm sample is under-represented by ~ 33 per cent. As shown in Fig. 12, all LBGs in HDFN with $[3.6] < 23$ are detected at 8.0 μm while for the shallower fields the number of LBGs lacking

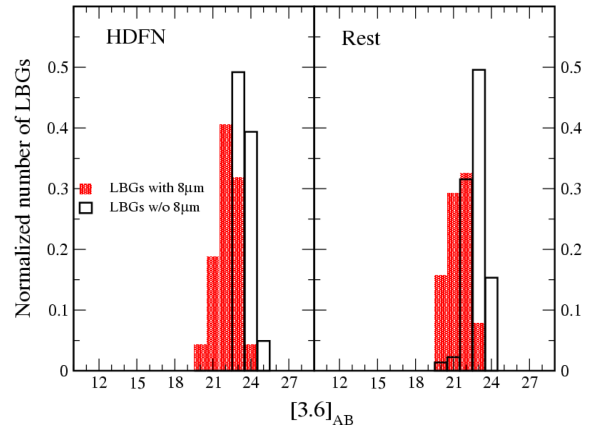


Figure 12. Normalized $[3.6]$ mag distribution of detected LBGs for LBGs with and without 8- μm detection (red and black bars, respectively). The left-hand panel shows the distribution for HDFN, while the right-hand panel shows the distribution for the rest of the fields.

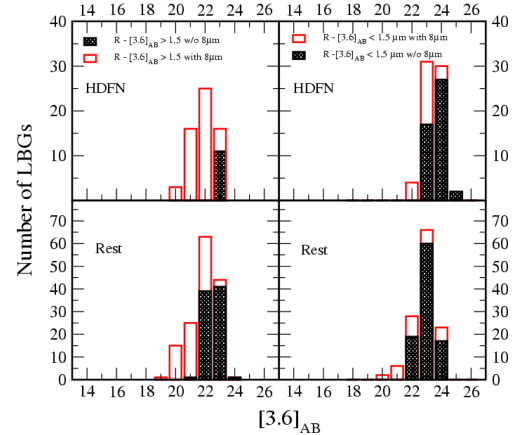


Figure 13. Upper left-hand panel: This figure shows how the ‘red’ LBGs, with and without 8- μm detection (red and black bars, respectively) are distributed in $[3.6]$ mag bins. Lower left-hand panel: Same as the upper left-hand panel, but for the rest of the fields. Upper right-hand panel: Same as the upper left-hand panel but for the ‘blue’ LBGs detected in HDFN. Lower right-hand panel: Same as the upper right-hand panel but for the rest of the fields.

8- μm counterpart at $[3.6] \sim 23$ are comparable with those detected at that band. We can therefore assume that the LBGs in the shallower fields having $[3.6] < 23$ but not detected at 8 μm do have an 8- μm counterpart but the observation was not deep enough to be detected. This is the minimum estimation of the undetected LBGs at 8 μm , as the fraction of detected/undetected at 8 μm remains higher for HDFN for the whole range of $[3.6]$ mag.

This non-detection of 8 μm mainly affects the $R - [3.6] > 1.5$ population of the sample and this is shown clearly in Fig. 13. According to the previous analysis, there are ~ 40 LBGs in the shallower fields with $R - [3.6] > 1.5$ that should have been detected at 8 μm , while for the $R - [3.6] < 1.5$ the missing LBGs are ~ 18 . If we regard those LBGs as detected at 8 μm , we find that that the median $< R - [3.6] >$ colour is 1.81 ± 0.164 with median $[3.6]$ value 22.47 ± 0.059 , while for those without 8- μm counterpart is 1.09 ± 0.26 with $[3.6]$ median 23.58 ± 0.187 (Fig. 14).

The significance of the 8- μm sample is that for $z \sim 3$, 8 μm correspond to K rest frame, sensitive to the bulk of the stellar emission of a galaxy and not only to the young population of a

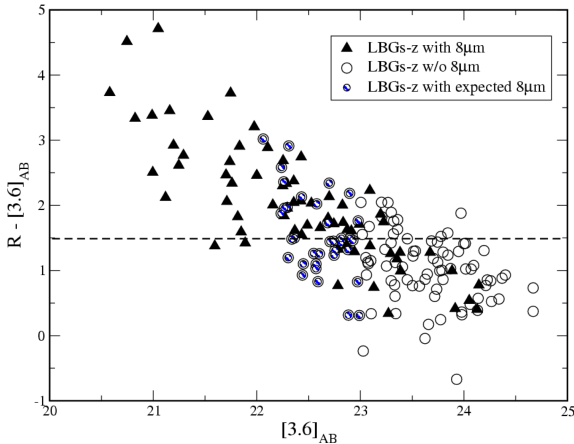


Figure 14. LBGs-z with 8.0- μm counterparts (triangles) exhibit redder $R - [3.6]$ colours compared to those undetected in 8.0 μm (empty circles). Shaded circles represent the LBGs of the fields with shallow depth that were not detected at 8 μm but we expect that with an exposure time similar to that of the HDFN would have been shown up at this band. If those LBGs are considered as detected at 8 μm , the mean value of LBGs with 8.0- μm counterpart is 1.81 (± 0.164) while for those not detected at 8.0 μm is 1.09 (± 0.26), respectively. The horizontal dashed line corresponds to $R - [3.6] = 1.5$.

recent star-forming event. In the first study of *Spitzer* detection of LBGs-z, Rigopoulou et al. (2006) suggests that LBGs-z detected in 8- μm band are dustier, more massive and relatively older than those with no detection. But her sample was small, covering LBGs-z from the EGS field. To put the Rigopoulou results on a secure statistical footing, in a forthcoming paper we use the current sample to constrain the physical properties of the LBGs-z and investigate the origin of the 8- μm emission.

4.3 Infrared colours of LBGs

As discussed before, LBGs exhibit a much wider range of flux densities in the IRAC bands than in the rest-UV. Fig. 8 shows that the range of 3.6- μm flux densities for the LBGs spans 6 mag, compared to only 3 mag for the range of rest-UV-band flux density. To investigate the IR colours of the LBGs, stellar synthesis population models can be employed. Fig. 15 compares the observed LBG colours with those predicted by two simple stellar population synthesis models generated with the new Charlot & Bruzual code that includes an observationally calibrated asymptotic giant branch (AGB) phase (Bruzual & Charlot, private communication). We considered both single-burst and constant star formation models, assuming solar metallicity and Salpeter IMF. These two models correspond to two extreme cases of a model having an exponentially decaying star formation rate, $\Psi(t) = e^{-t/\tau}$ where $\tau = 0.1$ is the single-burst model and $\tau = \infty$ is the constant star formation model. The model SEDs were generated for dust free and $E(B - V) = 0.3$ and for a grid of ages, ranging from 1 Myr to 2 Gyr. They were then redshifted at $z \sim 3$ matching the predicted $[3.6] - [4.5]$ and $R - [3.6]$ colours of star-forming galaxies. Although colour-colour diagrams are not the best way to constrain the properties of the stellar populations of a given galaxy class as one would have more free parameters than data points, we note that a combination of the two models with varying amounts of dust attenuation could reproduce the majority of the LBGs (with spectroscopic redshift) colours. This plot also shows that most of the LBGs without spectroscopic redshift, do have colours that are consistent with a galaxy at $z \sim 3$, while stars can be screened out

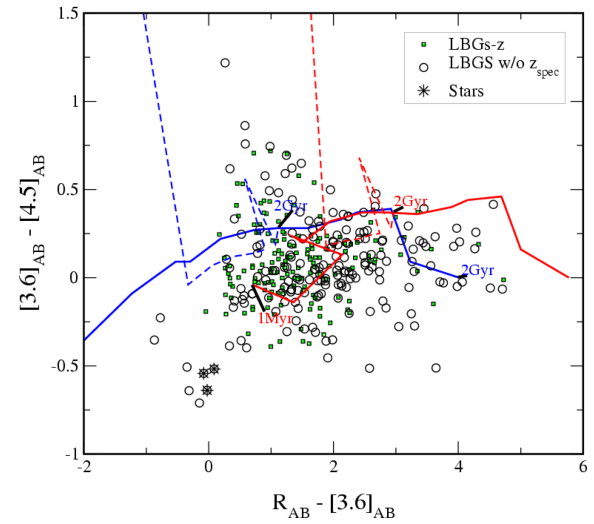


Figure 15. Observed frame $[3.6] - [4.5]$ versus $R - [3.6]$ colour-colour diagram for all LBGs detected with IRAC. Green squares represent LBGs with spectroscopic redshifts, circles represent LBGs without spectroscopic redshift, while asterisks represent stars. The lines show colours from stellar synthesis models based on Bruzual & Charlot (private communication): solid lines are the single-burst models, and dashed lines are the constant star formation models. The blue lines are dust-free models, and the red lines are models with $E(B - V) = 0.3$ and a Calzetti et al. (2000) reddening law. The single-burst models run from 1 Myr at the blue end of the line for the reddened model, off the plot for the dust-free model to 2 Gyr as indicated at the red end of the dashed lines. The constant star formation models, run from 100 Myr, off the plot for both dust-free and reddened model, to 2 Gyr as indicated in the red end of the solid lines. Overall the set of models spans nearly the entire colour range of the data.

from their blue $[3.6] - [4.5]$ colours. A more detailed study to estimate the stellar masses and the other physical properties of LBGs is currently undertaken based on model SEDs fitting (Magdis et al., in preparation).

4.4 Energy source in LBGs

The IRAC colours can also be used as an indicator, to separate luminous $z \sim 3$ AGN dominated objects from normal star-forming galaxies. The fraction of LBGs in our sample with spectroscopically identified AGN is 8/615. Fig. 16 shows that AGN (filled squares) occupy a distinct region in the $[4.5] - [8.0]$ over $[8.0]$ colour-magnitude plot when compared to LBGs. AGN are brighter in 8 μm and exhibit redder $[4.5] - [8.0]$ colours. The average $[4.5] - [8.0]$ colour for AGN is 1.22 ± 0.087 and for star-forming galaxies is 0.07 ± 0.22 while the average $[8.0]$ is 20.09 ± 0.04 and 22.32 ± 0.11 , respectively. Although most LBGs exhibit similar $[4.5] - [8.0]$ colours, those with $[4.5] - [8.0] < -0.5$ must represent a few really young LBGs with blue rest-frame $J - K$ colours, while those with $[4.5] - [8.0] \geq 1.0$ must represent the ILLBGs (Huang et al. 2005) with 24- μm detection as they are bright at 8 μm . The physical reason behind this diagnostic tool, is discussed by several authors (Ward et al. 1987; Elvis et al. 1994; Ivison et al. 2004). The SED of an AGN rises with a constant slope at the 0.1–10 μm rest-frame interval, while for a star-forming galaxy the SED is rather flat between rest 1 and 3 μm and then rises steeply towards longer wavelengths. IRAC bands at $z \sim 3$, correspond to rest-NIR (i.e. 0.9–2 μm), so we expect that that AGN should exhibit redder $[4.5] - [8.0]$ colours than young star-forming galaxies. Also, an AGN dominated object

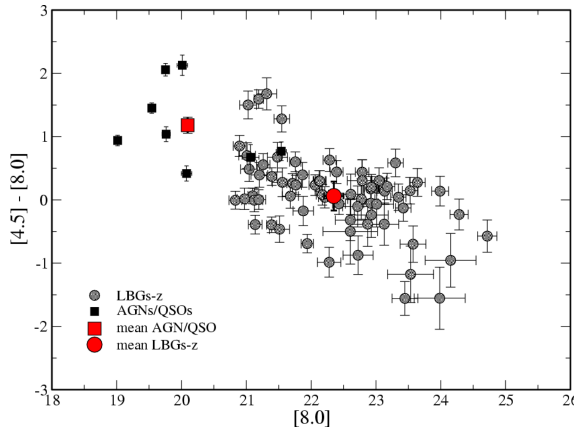


Figure 16. Colour–magnitude diagram of $[4.5] - [8.0]$ versus $[8.0]$. A colour–magnitude diagnostic plot for weeding out AGN. AGN (black squares) occupy a distinct area in that plot having redder $[4.5] - [8.0]$ colours and being brighter in $[8.0]$ band when compared to the LBG population (shaded circles). The red square and circle represent the average colour of AGN and LBGs-z, respectively, with AGN having average $[4.5] - [8.0]$ colour of $1.22 (\pm 0.087)$ and LBGs-z $0.07 (\pm 0.22)$.

is expected to have warmer dust and therefore having brighter $8\text{-}\mu\text{m}$ counterpart. Although a number of works are now showing that the *Spitzer* selection techniques do miss a large population of the X-ray selected population of AGN at intermediate X-ray luminosities (i.e. AGN with $L_x < \sim 10^{44} \text{ erg s}^{-1}$) (e.g. Barmby et al. 2006; Rigby et al. 2006), Reddy et al. (2006) showed that compilation of multiwavelength data for 11 AGN in HDFN indicates that optical and *Spitzer* data are able to efficiently (in terms of integration time) select high-redshift ($z \sim 3$), luminous AGN. Optical spectra and *Spitzer* and *Chandra* data are all required to fully account for the census of AGN at high redshifts.

5 SUMMARY AND CONCLUSIONS

Through the photometric analysis of six fields covered by all four IRAC bands onboard *Spitzer* our conclusions are as follows.

- (i) The excellent agreement of the number counts between all the fields in the bright end and between observations of equal exposure time in the faint end shows that our photometric technique and source extraction has treated all fields in the same manner.
- (ii) Out of ~ 700 LBGs that were covered by our data, 443, 448, 137 and 152 LBGs were identified at 3.6-, 4.5-, 5.8-, 8.0- μm IRAC bands, respectively, creating the largest existing rest-NIR sample of high-redshift galaxies.

(iii) The SED of the LBGs were expanded to NIR and show that the NIR colours of the population spans over 6 mag. The addition of IRAC bands reveals for the first time that LBGs display a variety of colours and their rest-NIR properties are rather inhomogeneous, ranging from

- (1) those that are bright in IRAC bands and exhibit $R - [3.6] > 1.5$ colours with steeply rising SEDs towards longer wavelengths to
- (2) those that are faint or not detected at all in IRAC bands with $R - [3.6] < 1.5$ colour whose SEDs are rather flat from the far-UV to the NIR with marginal IRAC detections.

(iv) Out of the whole sample, ~ 20 per cent of the LBGs are detected at $8.0 \mu\text{m}$. We refer to them as the $8.0\text{-}\mu\text{m}$ sample of LBGs (it is equivalent to a rest-frame K -selected sample). Those LBGs tend to have redder $R - [3.6]$ colours when compared to the rest

population with median values of $1.81 (\pm 0.16)$ and $1.09 (\pm 0.26)$, respectively.

(v) The IR colours of LBGs are consistent with those of $z \sim 3$ galaxies and indicating that their SEDs are can be fitted with various stellar synthesis population models. The mid-IR properties of the LBG (i.e. masses, dust, age link to other $z \sim 3$ galaxy populations) will be presented in detail in a forthcoming paper as well as the full photometric catalogues.

(vi) Based on results for a few $z \sim 3$ optically identified AGN, IRAC $8\text{-}\mu\text{m}$ band can be used as a diagnostic tool to separate luminous, high- z , AGN dominated objects from star-forming galaxies with AGN being brighter in $[8.0]$ band when compared to the LBG population.

ACKNOWLEDGMENTS

This work is based on observations made with the *Spitzer Space Telescope*, which is operated by the Jet Propulsion Laboratory, California Institute of Technology under a contract with NASA. Support for this work was provided by NASA through an award issued by JPL/Caltech.

REFERENCES

- Adelberger K. L., Steidel C. C., 2000, ApJ, 544, 218
- Arnouts S. et al., 2001, A&A, 379, 740
- Bell E. F., deJong R. S., 2001, ApJ, 550, 212
- Barmby P. et al., 2004, ApJS, 154, 97B
- Barmby P. et al., 2006, ApJ, 642, 126B
- Bertoldi F. et al., 2000, A&A, 360, 92B
- Calzetti D., Armus L., Bohlin R. C., Kinney A. L., Koornneef J., Storchi-Bergmann T., 2000, ApJ, 533, 682
- Chapman S. C. et al., 2000, MNRAS, 319, 318
- Chapman S. C., Blain A. W., Smail I., Ivison R. J., 2005, ApJ, 622, 772
- Daddi E., Cimatti A., Renzini A., Fontana A., Mignoli M., Pozzetti L., Tozzi P., Zamorani G., 2004, ApJ, 617, 746
- Elvis M., Fiore F., Wilkes B., McDowell J., Bechtold J., 1994, ApJ, 422, 60
- Fazio G. G. et al., 2004, ApJS, 154, 10
- Franceschini A. et al., 2006, A&A, 453, 397
- Franx M. et al., 2003, ApJ, 587, L79
- Huang J.-S. et al., 2004, ApJS, 154, 44
- Huang J.-S. et al., 2005, ApJ, 634, 137
- Hughes D. et al., 1998, Nat, 394, 241
- Ivison R. J. et al., 2002, MNRAS, 333, 1I
- Ivison R. J. et al., 2004, ApJS, 154, 124I
- Lilly S. J., Eales S. A., Gear W. K. P., Hammer F., Le Fèvre O., Crampton D., Bond J. R., Dunne L., 1999, ApJ, 518, 641
- Nandra K., Mushotzky R. F., Arnaud K., Steidel C. C., Adelberger K. L., Gardner J. P., Teplitz H. I., Windhorst R. A., 2002, ApJ, 576, 625
- Papovich C., Dickinson M., Ferguson H. C., 2001, ApJ, 559, 620
- Pettini M., Shapley A. E., Steidel C. C., Cuby J.-G., Dickinson M., Moorwood A. F. M., Adelberger K. L., Giavalisco M., 2001, ApJ, 554, 981
- Reddy N. A., Steidel C. C., 2004, ApJ, 603, L13
- Reddy N. A., Steidel C. C., Fadda D., Yan L., Pettini M., Shapley A. E., Erb D. K., Adelberger K. L., 2006, ApJ, 644, 792
- Rigby J. R., Rieke G. H., Donley J. L., Alonso-Herrero A., Pérez-González P. G., 2006, ApJ, 645, 115R
- Rigopoulou D. et al., 2006, ApJ, 648, 81R
- Sawicki M., Yee H. C., 1998, AJ, 115, 1329
- Shapley A. E., Steidel C. C., Adelberger K. L., Dickinson M., Giavalisco M., Pettini M., 2001, ApJ, 562, 95
- Shapley A. E., Steidel C. C., Pettini M., Adelberger K. L., 2003, ApJ, 588, 65
- Shapley A. E., Steidel C. C., Erb D. K., Reddy N. A., Adelberger K. L., Pettini M., Barmby P., Huang J., 2005, ApJ, 626, 698

- Smail I., Ivison R. J., Blain A. W., Kneib J.-P., 2002, MNRAS, 331, 495S
Steidel C. C., Hamilton D., 1993, AJ, 105, 2017
Steidel C. C., Adelberger K., Giavalisco M., Dickinson M., Pettini M., 1999,
ApJ, 519, 1
Steidel C. C., Adelberger K. L., Shapley A. E., Pettini M., Dickinson M.,
Giavalisco M., 2003, ApJ, 592, 728
Vijh U. P., Witt A. N., Gordon K. D., 2003, ApJ, 587, 533
- Ward M., Elvis M., Fabbiano G., Carleton M.-P., Willner L. P., Lawrence
K., 1987, ApJ, 315, 74
Werner M. W. et al., 2004, ApJS, 154, 1
Wilson G. et al., 2004, ApJS, 154, 107

This paper has been typeset from a $\text{\TeX}/\text{\LaTeX}$ file prepared by the author.